JOURNAL OF GEOPHYSICAL RESEARCH, VOL. 92, NO. C6, PAGES 6521–6534, JUNE 15, 1987

A Microwave Radiometer Weather-Correcting Sea Ice Algorithm

J. M. WALTERS, C. RUF, AND C. T. SWIFT

Department of Electrical and Computer Engineering, University of Massachusetts, Amherst

An algorithm is developed which uses six channels of the Scanning Multichannel Microwave Radiometer to estimate fractions of multiyear and first-year sea ice types under variable atmospheric and sea surface conditions. Previously published sea ice algorithms have used a minimal number of channels and have therefore avoided most problems associated with noisy data as well as detailed atmospheric correction. Algorithms used for retrieval of atmospheric parameters concentrate on a statistical approach utilizing as many channels as possible. The present work attempts to synthesize these two classes of algorithms by using several radiometer data channels. This algorithm is specifically tuned to derive sea ice parameters while accepting error in the auxiliary parameters of surface temperature, ocean surface wind speed, atmospheric water vapor, and cloud liquid water content. The four additional environmental parameters are derived only for the purpose of correcting the sea ice parameters at the expense of accepting absolute errors in the derivation of the secondary parameters. These large errors propagate small errors in the resultant sea ice fractions. This weather-correcting algorithm performs at least as well, if not better, than the first-generation algorithms over consolidated ice and appears to perform very well when the sea ice concentration is less than 20%. To this end, the results are compared with the results of two algorithms that appear in the published literature. Unlike one of the algorithms that employs a weather filter, this new algorithm utilizes the radiative transfer equation to correct for these effects and thus eliminates false retrievals of sea ice without discarding data. The penalty that is paid is that more computer resources are required.

INTRODUCTION

Over the past 15 years there has been increasing awareness of the ability of microwave instruments to distinguish between different types of sea ice and water within their footprint. This has evolved from experiments of the 1970s, such as the Arctic Ice Dynamics Joint Experiment that utilized aircraft and shipborne devices, to present experiments where satellite instruments, such as the Seasat and Nimbus 7 Scanning Multichannel Microwave Radiometer (SMMR) provide the data. This research has shown that passive microwave radiometers provide synoptic measurements of ice concentration in a timely manner and with accuracy hitherto unattainable.

At the present time, three groups have developed algorithms to retrieve sea ice parameters from SMMR data: the University of Massachusetts/Atmospheric Environment Service (UMass-AES) [*Swift, Fedor, and Ramseier*, 1985], NASA Goddard (Nimbus team) [*Cavalieri, Gloersen, and Campbell*, 1984], and the University of Bergen (NORSEX) [*Svendsen et al.*, 1983]. These efforts on remote sensing of sea ice focus on simple algorithms for purposes of computational efficiency, thus no correction is made for effects of local weather conditions on the measured satellite parameters. One exception is the implementation of a weather filter which enhances the ice edge and reduces false retrievals of sea ice in areas of the world where there can be no sea ice [*Gloersen and Cavalieri*, 1986]. The basis of the UMass-AES algorithm is to linearize the radiative transfer equation and then to assume that both temperature and weather effects are constant biases in the data which can be removed by calibration techniques or accepted as error. This algorithm uses only the 18- and 37-GHz data channels. The use of only one polarization, specifically, the vertical polarization, also reduces the effects of rough surfaces. Although this algorithm is quite simple, it still yields estimates of the ice fraction within about 10%. However, as will be shown in this paper, open water areas yield a 10–20% uncertainty, which leads to false retrievals and loss of detail relating to ice concentration at the ice edge. This algorithm also requires that the surface temperature of the target area be known to within 10 K. Another approach to the ice concentration problem was developed by the Nimbus 7 team. In an effort to reduce both temperature and weather effects, this algorithm uses various combinations of brightness temperature ratios. Typically, three or four data channels are used to retrieve the same amount of information, but the results are relatively insensitive to variations in ice surface temperature. The Nimbus team algorithm uses the spectral gradient ratio to suppress weather-related effects over the open ocean [*Gloersen and Cavalieri*, 1986]. This reduces the ice edge noise seen in the UMass-AES algorithm but also neglects real data when the ice concentration is less than 8–12%. Due to the ratio technique used this algorithm is more sensitive to instrument noise; however, the precision of the sensors is such that the random error contributes less than $\pm 5\%$ retrieval errors in ice concentration [*Swift and Cavalieri*, 1985]. The NORSEX algorithm is similar to the UMass-AES algorithm in the sense that only two data channels are required. The major difference is that an ad hoc procedure is used to estimate the ice surface temperature from buoys that measure air temperature. The NORSEX algorithm produces results of the same accuracy as the UMass-AES algorithm; however, some initial input surface temperature values are required. This dependence on external data input from buoys reduces the overall operational advantage of the algorithm. A more detailed comparison of the algorithms is presented by *Swift and Cavalieri* [1985].

All three of these algorithms are subject to common errors through the assumption that the sea ice composition within the footprint of the radiometer consists of only three components, namely, open water, first-year sea ice, and multiyear sea ice. In fact, it is well known that other ice types, such as nilas, occur during the growth process which may influence the radiating properties of the mixture. At the present time there is

Paper number 7C0224.
0148-0227/87/007C-0224$05.00

inconclusive evidence to indicate that SMMR data can distinguish these other ice types from the three principal components presently being retrieved by the existing algorithms. As a result, the formulation presented herein will also assume that the surface consists of only three components. Unlike the previous first-generation algorithms which used no more than two or three SMMR channels the algorithm described herein utilizes all six SMMR channels that provide an effective spatial resolution of 50 km. Specifically, 18-, 21-, and 37-GHz horizontally and vertically polarized channels are used to retrieve the following six environmental unknowns: total water (or ice) fraction, multiyear sea ice fraction, surface temperature, ocean surface wind speed, integrated atmospheric water vapor, and cloud liquid water content. The algorithm is specifically tuned to retrieve sea ice parameters at the expense of accepting absolute error in the retrieval of all other environmental errors. The purpose is to shift systematic errors, for example, those coupled with instrument biases, to secondary parameters, yet providing corrections that may yield an improved sea ice product.

The assignment of absolute errors to the derived sea ice product will require more research activity. However, our preliminary evaluation indicates that the weather-correcting algorithm provides a better data product than the UMass-AES algorithm, whose quality has been cross checked with independent surface observations. Not only does the algorithm naturally correct for changes in local weather conditions, but it is specifically tuned to retrieve sea ice parameters to the extent that gross errors in atmospheric conditions propagate small errors into the sea ice retrievals. As a case in point, the atmospheric model, as initially formulated, was in error by a factor of 2 in an exponential, yet an error of only 1% was propagated into the sea ice retrieval.

ALGORITHM DEVELOPMENT

The basic relationship between physical parameters and microwave radiometer measurements is the radiative transfer equation. The integral form of this relationship is

$$T_b = T_c r e^{-2\tau_\infty} + T_{\text{air}} r e^{-\tau_\infty} + (1-r) T_s e^{-\tau_\infty} + T_{\text{air}} \tag{1}$$

where

$$T_{\text{air}} = \int_0^{\tau_\infty{}^0} T(z) e^{-\tau(z)\sec\theta}\, d[\tau(z)\sec\theta] \tag{2}$$

and where T_b is the observed brightness temperature measured in degrees Kelvin, T_c is equal to 2.7 K the cosmic background radiation, r is the actual surface reflectivity, T_s is the actual surface temperature measured in degrees Kelvin, $\tau_\infty{}^0$ is the one-way zenith atmospheric opacity seen by the satellite, τ_∞ is equal to $\tau_\infty{}^0 \sec\theta$, the line of sight opacity measured from zenith, $T(z)$ is the true air temperature in degrees Kelvin at height z, and T_{air} is the apparent temperature of the air column.

Replacing the $T(z)$ in (2) by a constant value $\langle T\rangle$, the average columnar air temperature (2) can be simplified to

$$T_{\text{air}} = \langle T\rangle (1 - e^{-\tau_\infty}) \tag{3}$$

and then substituting (3) into (1), we arrive at

$$T_b = \langle T\rangle - r e^{-2\tau_\infty}(\langle T\rangle - T_c) + (1-r)(T_s - \langle T\rangle) e^{-\tau_\infty} \tag{4}$$

Equation (4) is the simplified version of the radiative transfer equation which is the basis of the weather-correcting algorithm developed herein. Equation (4) can be solved for r in terms of $\langle T\rangle$, T_s, T_b, and τ_∞ yielding

$$r = \frac{(\langle T\rangle - T_b) + e^{-\tau_\infty}(T_s - \langle T\rangle)}{(\langle T\rangle - T_c) e^{-2\tau_\infty} + e^{-\tau_\infty}(T_s - \langle T\rangle)} \tag{5}$$

This relationship is used to solve for the reflectivity at each of the data channels. Values for T_s, $\langle T\rangle$, and τ_∞ are solved by iteration, as discussed in a subsequent section of the paper.

Current practice in sea ice concentration algorithms is to model the surface as a composite of three distinct surface types: water, first-year ice, and multiyear ice. Each of these components is assigned a fractional concentration. This represents the portion of the footprint which is covered by each of the three types. As a result of this division, we can form the following relationship, which will hold whenever the surface is defined only by these three components.

$$f_w + f_{fy} + f_{my} = 1 \tag{6}$$

At microwave frequencies each of these surface components have different emission characteristics, allowing a differentiation between them based upon reflectivities. Due to the averaging nature of radiometric observation the composite reflectivity will be represented as

$$r = r_w f_w + r_{fy} f_{fy} + r_{my} f_{my} \tag{7}$$

where r_w, r_{fy}, and r_{my} are the component reflectivities corresponding to 100% water, first-year sea ice, and multiyear sea ice, respectively. As a means to reduce the total unknowns, (7) assumes that the ice and water temperature are the same. As shown in the Appendix, this assumption is judged to cause negligible error as a result of the constraints imposed upon the surface temperature.

The method used to determine these reflectivities is based on cluster analysis techniques as advanced by *Comiso* [1983] and others and is discussed in the following section of this paper. Table 1 lists the surface reflectivities for the appropriate SMMR channels as derived by this cluster method. Because of instrument biases these are not true surface reflectivities but rather calibration points for the algorithm.

The reflectivities r_{fy} and r_{my} are assumed to be constant over the entire polar region. Other factors such as ice roughness, snow cover, and thin ice types may cause variability in these values and resultant errors which are not presently quantified. The term r_w is not a constant, as it varies significantly with ocean surface wind speed and to some extent with the surface temperature. This relationship can be expressed as

$$r_w = r_w{}^c + r_w{}^t(T_s) + r_w{}^u(u) \tag{8}$$

where $r_w{}^c$ is the reflectivity of calm sea water at temperature

TABLE 1. Surface Reflectivities

Frequency, GHz	Polarization	Reflectivity: Calm Water	First-Year Ice	Multiyear Ice
18	horizontal	0.680	0.136	0.264
	vertical	0.412	0.092	0.166
21	horizontal	0.666	0.133	0.267
	vertical	0.394	0.090	0.180
37	horizontal	0.591	0.108	0.328
	vertical	0.301	0.075	0.252

T_0, u is the wind speed measured in meters per second, r_w^u is the change in reflectivity due to wind effects, and r_w^t is the change in reflectivity due to temperature effects. The term r_w^c can be computed theoretically [*Klein and Swift*, 1977] or determined from the cluster diagrams. The values used for r_w^t are derived from the Klein-Swift equations, which can be modeled as:

$$r_w^t(T_s) = c_w^t(1 - e^{-(T_s - 270)/20}) \quad (9)$$

The empirical coefficient c_w^t is computed for each channel by a least squares fit to the Klein-Swift model. The relative accuracy of this approximation is better than 2% for all six data channels used.

Wentz [1983] has derived values for r_w^u from available Seasat data. At low frequencies, $r_w^u(u)$ appears to be nonlinear, but for higher frequencies such as 18, 21, and 37 GHz it can be formulated in a linear fashion $r_w^u(u) = c_w^u \cdot u$, where c_w^u is a constant dependent on frequency and polarization. The quantity u represents the frictional wind velocity and is linearly proportional to the wind speed for low wind speeds. This linear relationship will be assumed for all wind speeds in an effort to simplify analysis of the output.

A term δu is added at this point to allow for an iterative solution for the wind vector u. This is done by allowing δu to become part of the surface solution vector, which represents a first-order solution, while u_0 is properly a part of the solution for r_w.

Substituting (8) and (9) into (7) and including the expression for u_0, the total reflectivity can be represented as

$$r = f_w(r_w^c + c_w^t(1 - e^{-(T_s - 270)/20}) + c_w^u u_0) + f_{fy} r_{fy} + f_{my} r_{my} + r_w^u \delta u \quad (10)$$

This equation is first order in f_w, f_{fy}, f_{my}, and u if T_s is assumed to be a known parameter. Indeed, T_s is determined at a later stage of the algorithm, and new reflectivities are solved by iteration. The values used for r_w^c, r_{fy}, and r_{my} were shown in Table 1, and the values for c_w^t and c_w^u are given in Table 2. The last term in (10) becomes negligible when the iteration is complete. The iteration procedure overspecifies the problem by using all six SMMR channels to solve for four unknowns.

The model of atmospheric attenuation used in this algorithm is a scaled down version of that advanced by *Wentz* [1983]. The Wentz model assumes that the atmospheric opacity is due to oxygen attenuation, the attenuation due to water vapor, and the attenuation due to cloud droplets and rain. The model also assumes that each parameter is a function of temperature and optical depth. In order to reduce the number of unknowns in our algorithm, rain attenuation is assumed to be the same as cloud droplets, and the functional dependence on temperature and optical depth is neglected.

The basic form of the Wentz model of atmospheric opacity

TABLE 2. Weather Effect Reflectivity Coefficients

Frequency, GHz	Polarization	c_w^t	c_w^u
18	horizontal	0.05438	0.00337
	vertical	0.07806	0.00127
21	horizontal	0.06386	0.00362
	vertical	0.08965	0.00128
37	horizontal	0.1006	0.00502
	vertical	0.1258	0.00134

TABLE 3. Integrated Atmospheric Absorption Coefficients at Zenith

Frequency, GHz	Oxygen, A, nepers	Vapor, B, nepers/g/cm^2	Liquid, C, nepers/g/cm^2
18	0.019	0.027	2.250
21	0.022	0.091	2.720
37	0.058	0.047	4.448

1 neper = (0.1 ln 10) × 1 dB attenuation.

is

$$2\tau_\infty{}^0 = A + BV + CL \quad (11)$$

where A, B, and C are constants which depend upon frequency as given in Table 3, and $\tau_\infty{}^0$ is the opacity at zenith. The quantities V and L are, respectively, the integrated atmospheric water vapor and liquid water in grams per square centimeter.

Several researchers [*Wentz*, 1983; *Wilheit and Chang*, 1980; *Gloersen and Barath*, 1977], to name a few, have developed algorithms to retrieve atmospheric parameters over the ocean, which is possible because the reflectivity of water is high and therefore provides a relatively cold background. Due to the low reflectivity of ice at microwave frequencies this retrieval is much more difficult. It is the application of the open water atmospheric parameter retrieval methods to the sea ice concentration problem that this paper addresses. However, unlike other work on atmospheric retrievals over the ocean the interest is in correcting errors in the surface retrievals, and absolute accuracy of atmospheric parameters is not of primary concern here.

All three of the sea ice algorithms discussed earlier have used a minimal number of channels to retrieve surface parameters and have therefore avoided most of the problems of noisy data as well as the detailed atmospheric correction (the Goddard algorithm implements a weather filter). Only the 18- and 37-GHz channels have been used which, while providing high surface resolution, have the disadvantage of being susceptible to weather effects. Algorithms used for the retrieval of atmospheric parameters concentrate on a statistical approach utilizing as many channels as possible, generally forming a linear relationship between environmental parameters and brightness temperature. The present work attempts to synthesize these two types of algorithms by using several high-frequency channels, including the 21-GHz channel to provide atmospheric water vapor information.

ALGORITHM CALIBRATION POINTS

Ideally, the component reflectivities can be predetermined from aircraft or ground-based measurement programs. Unfortunately, such a strategy has never proven to be completely adequate for reasons including insufficient sampling and unknown instrument to instrument biases. As a result, a clustering method [*Comiso*, 1983; *Swift et al.*, 1985; *Gloersen and Cavalieri*, 1986] has been advanced to use the satellite data itself to infer the component reflectivities. The advantages of the method are that thousands of data points can be gathered in a short period of time from satellite platforms to satisfy sampling requirements, and equivalent component reflectivities can be derived to self correct for the instrument offsets.

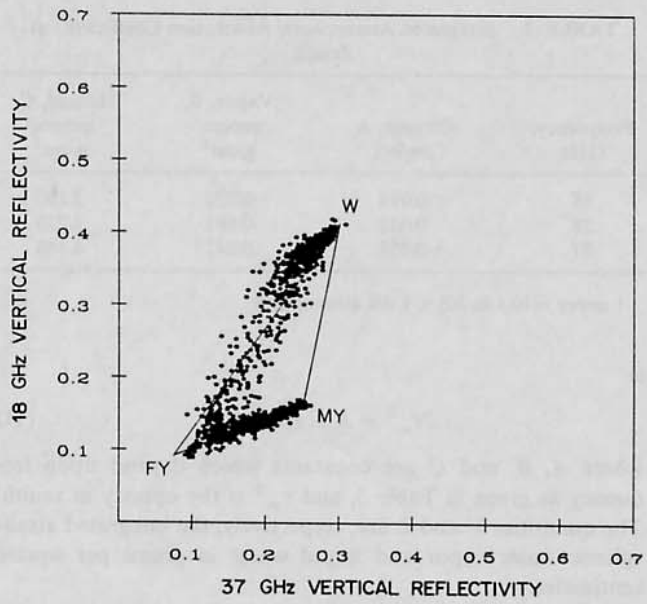

Fig. 1. A clustering of Seasat SMMR data points, reduced to surface reflectivity, for the 18- and 37-GHz vertically polarized channels. Shown in this curve is the triangle used to derive the reflectivities of water, first-year sea ice, and multiyear sea ice. The lower-left apex represents 100% first-year sea ice, the lower-right apex represents 100% multiyear sea ice, and the upper apex represents the reflectivity of calm water. Points lying outside the valid retrieval triangle are presumed to be due to weather and ocean surface effects.

The merit of this approach is discussed by *Swift et al.* [1985].

A typical cluster plot is shown in Figure 1, which cross plots processed data from the Seasat SMMR 18- and 37-GHz vertically polarized channels. This particular figure was generated from the Seasat SMMR brightness temperatures as processed through (5) assuming values of $T_s = 270$ K, $\langle T \rangle = 255$ K, and τ_∞ is the oxygen opacity. Note that no corrections are made for atmospheric attenuation due to water vapor or clouds. These corrections are not necessary at this stage because the only purpose here is to infer the respective effective reflectivities of 100% water, first-year, and multiyear sea ice. When two channels of SMMR data are cross plotted as in Figure 1, the data points generally follow an inverted figure seven shape. If a triangle is superimposed over the scatter points, a tightly bound set of data tends to follow the side of the triangle connecting the vertices labeled FY and MY. A second, and much less tightly bound cluster of points follows the line between vertices labeled FY and W to complete the inverted figure seven shape. As suggested by the figure labels, the FY-MY cluster represents varying concentrations of a first-year, multiyear sea ice mixture that contains very little water. Indeed, these data points are generally associated with the northern most pixels of the SMMR swath. Similarly, the FY-W line is associated with the SMMR data collected from the southern most pixels of the SMMR swath. Note that there are no points that cluster along the MY-W line because the probability of occurrence of only water and multiyear sea ice within a pixel is small.

The observation that data points are not tightly bound along the FY-W line motivated the development of the weather-correcting algorithm. A valid sea ice retrieval requires that all data points must lie within the inscribed triangle; otherwise, the algorithm will retrieve component fractions greater than 100% and less that 0%. We therefore conclude that the vast majority of points not inside the valid retrieval triangle are coupled with variable atmospheric and ocean surface conditions. Errors related to the latter have been discussed by *Gloersen and Cavalieri* [1986] and were addressed simply by discarding data points that cluster about the water vertex. Even with the implementation of this weather filter, other points that cluster outside the FY-W line result from variable atmospheric conditions and are accepted as error.

Although the cluster diagram illustrates the shortcomings of the first-generation sea ice algorithms, its real value here is to establish component reflectivities, or more precisely, the algorithm calibration points. Although weather and ocean surface effects impose restrictions on the sea ice retrievals, it seems reasonable to assume that out of thousands of data points clustered, some will correspond to clear atmosphere, calm water conditions with near 100% concentrations of each of the three components within the footprint. It is further argued that these points will lie near the vertices of the triangle. The vertices are therefore identified as the effective component reflectivities, and the derived values are given in Table 1.

Again, we emphasize that the values listed in Table 1 are not true reflectivities but rather, imposed calibration points that include effects of instrument biases. By selecting such calibration points, physically realizable sea ice concentrations are derived at the expense of accepting absolute error in the retrievals of other geophysical parameters such as surface temperature for which calibration points have not been established.

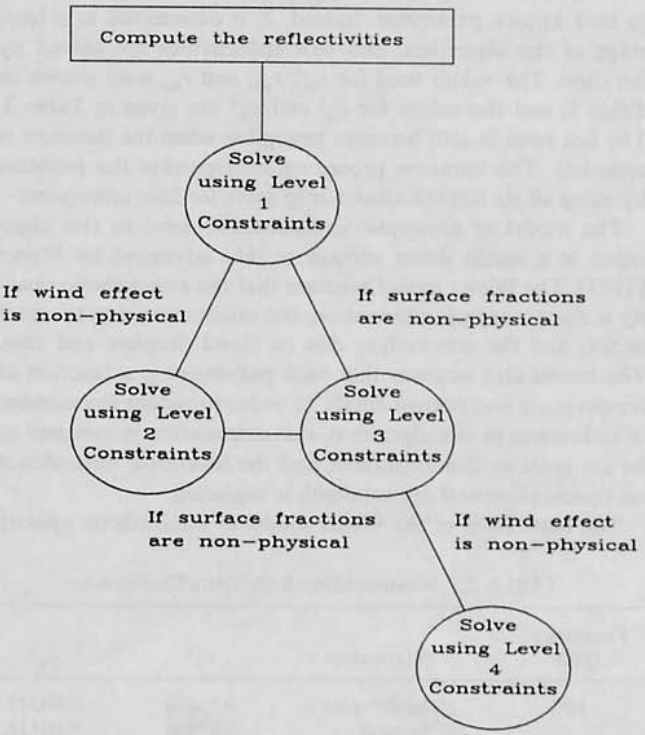

Fig. 2. A flow chart representing the level of constraints applied through Lagrange multipliers needed to achieve physically realizable retrievals of environmental parameters. The intent is to derive the least constrained solution.

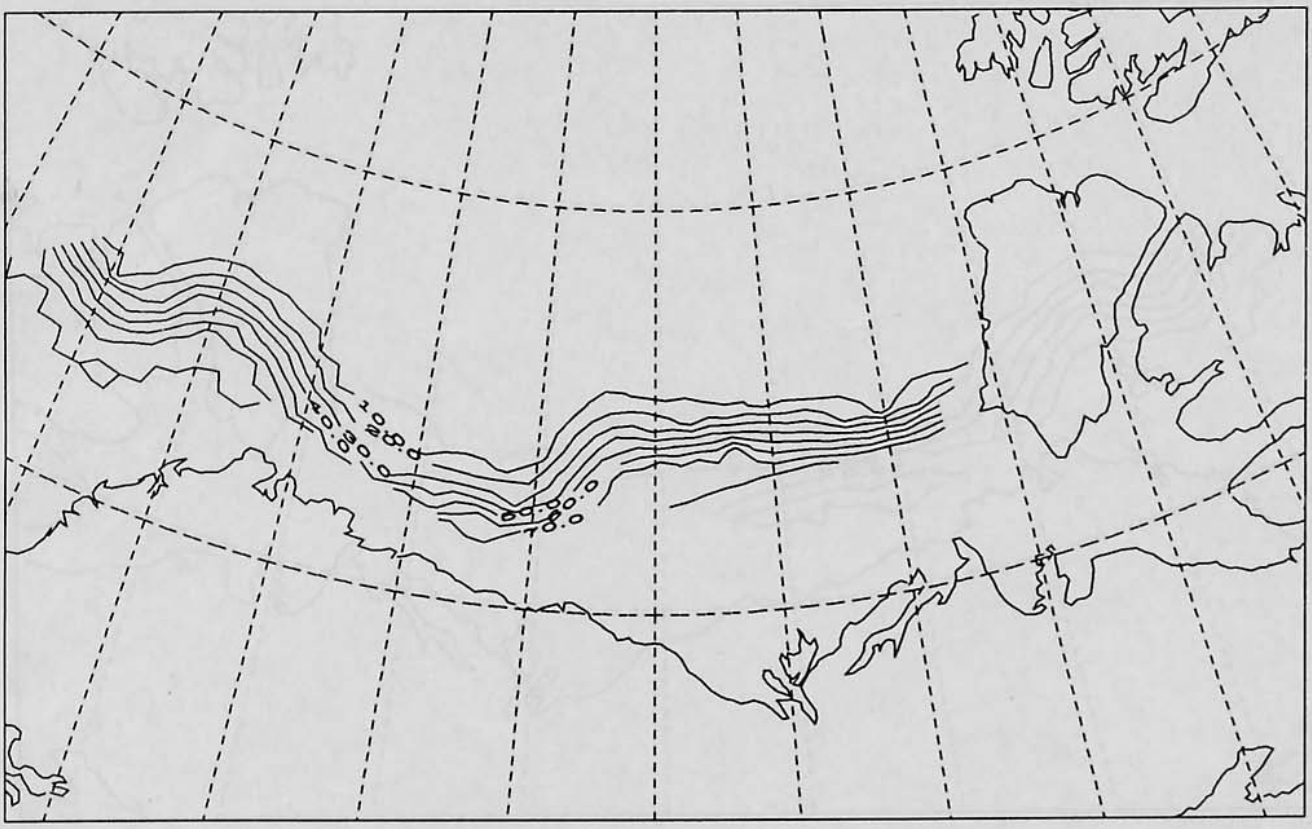

Fig. 3. Contours of surface water concentration as derived from the UMass-AES algorithms for Seasat orbit 1395 (October 2, 1978). The maximum concentration shown in the figure is 80% water.

ALGORITHM IMPLEMENTATION

The algorithm uses several matrices of parameters, and vectors to represent sets of interrelated quantities. The main focus of the algorithm is the surface parameter vector F. This vector consists of the ordered set $(f_w, f_{fy}, f_{my}, \delta u)$, provided the data are not contaminated by additional components such as land. The matrix R, which is defined by the component reflectivities given in Table 1, operates on the vector F, and from (10) can be seen to consist of one row per data channel, each row containing the appropriate ordered set $(r_w, r_{fy}, r_{my}, r_w^u)$. Defining the reflectivity vector r as the vector containing the composite reflectivities arranged in row order equivalent to the order used in the matrix R, (10) can be rewritten for the multichannel case in vector notation as

$$[R] \cdot [F] = [r] \tag{12}$$

This r vector is then the least squares fit reflectivity vector for the pixel with surface F. This algorithm considers F to be the unknown, and therefore the vector r must be related to known quantities using the following relationship:

$$[r] = [m] + [\Delta] \tag{13}$$

where m is the actual measured reflectivity vector computed using (5), and Δ is a difference vector which will be minimized by the least squares process.

Using (5), we can directly solve for the measured reflectivity m at any channel, and the matrix R, This leaves F and Δ as the unknown vectors in (13). In order to solve this system the difference vector Δ will be minimized with respect to F using vector calculus. Several constraints will be added to the solution in the form of Lagrange multipliers.

At this point the consideration of the various constraints used is in order. The first constraint is derived from (6), where

$$[F] \cdot [A] = 1 \qquad [A] = (1, 1, 1, 0) \tag{14}$$

This constraint simply forces the sum of the three surface fractions to add to one. The constraint will be applied by a Lagrange multiplier λ_0. For all cases this constraint applies; therefore it will always be a part of the solution.

The second constraint is related to the weather correction feature of the algorithm. In the previous section the valid retrieval triangle in reflectivity space was discussed. One problem with the first-generation algorithms is their inability to ensure that retrieved values lie within or on the edges of this triangle. In the weather-correcting algorithm if the initial value of the solution is not within or on the edge of the valid retrieval triangle, it will be constrained to lie somewhere along one of the edges. This constraint can be represented by the following:

$$[F] \cdot [B_i] = 0 \tag{15}$$

where $B_1 = (1, 0, 0, 0)$, $B_2 = (0, 1, 0, 0)$, and $B_3 = (0, 0, 1, 0)$. This constraint is physically reasonable, since the basic shape of the points in a cluster diagram is an inverted figure seven close to the edges of the valid retrieval triangle. This constraint is applied by the Lagrange multiplier λ_i, which may take on any of three values depending on i. These three different values correspond to the three sides of the valid retrieval

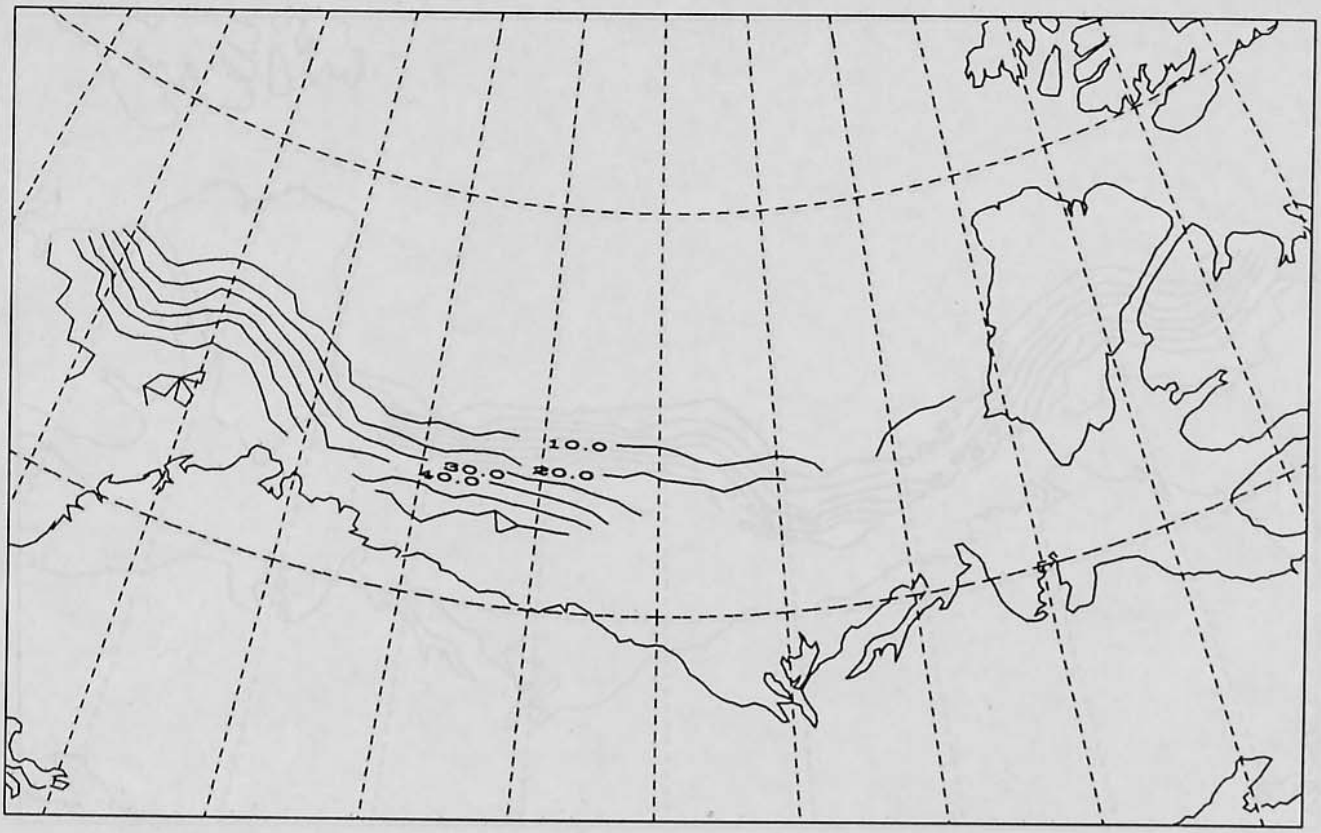

Fig. 4. Contour of surface water concentration as derived from the UMass-AES algorithm for Seasat orbit 1481 (October 8, 1978). A weather cell passed through the area a day before the data were collected and modified the distribution of sea ice as shown in Figure 3. The maximum concentration shown here is 70%.

triangle. In order to find the optimal solution it is necessary to compute all three solutions and find the one with the lowest error. In essence, this constraint forces positive concentrations not to exceed 100%.

The last constraint is a result of the method used to solve for the wind value u. Mathematically, u can take on any value positive or negative. However, u must be physically greater than or equal to zero. In order to constrain u it is necessary to ensure that u is, in fact, nonnegative. This is applied by the following method. A solution is found with no constraint on u, and if u is nonnegative, the solution is valid in u. If the solution is negative, then a constraint of $u = 0$ is applied and the system is solved again. This constraint is applied by the Lagrange multiplier λ_1, and is represented by

$$[F] \cdot [C] = -u_0 \qquad C = (0, 0, 0, 1) \tag{16}$$

The constraint forces $u = 0$ by setting $\delta u = -u_0$ so that $u = u_0 + \delta u = 0$.

Solving (13) in terms of Δ, taking the dot product of Δ with itself, and adding all of the constraints provides the following vector relationship of the algorithm.

$$(RF - m, RF - m) = (\Delta, \Delta) + \lambda_0{}^i[(F, A) - 1] + \lambda_i(F, B_i) + \lambda_1{}^i[(F, C) + u_0] \qquad (i = 1, 2, 3) \tag{17}$$

By differentiating this equation in terms of F, Δ will be minimized. Operating on (17) with the operator ∇_F and then solving the equation in terms of F yields

$$F = (R^tR)^{-1}R^tm + \lambda_0{}^i(R^tR)^{-1}A + \lambda_i(R^tR)^{-1}B_i + \lambda_1{}^i(R^tR)^{-1}C \tag{18}$$

where $i = (1, 2, 3)$. By employing the three constraints, each of the three Lagrange multipliers can be determined.

Iteration of the algorithm consists of the computation of the measured reflectivity vector m from (5), first using an initial value then the previous values of T_s, $\langle T \rangle$, and τ_∞, and the measured value of T_b. This allows a solution for the best fit F and r vector for the pixel. Using this best-fit-computed r vector for the pixel, new values of T_s, $\langle T \rangle$, and τ_∞ are simultaneously computed in accordance with the forthcoming discussion. Upon completion of this activity for all pixels the entire matrix of T_s and τ_∞ is passed through a low-pass filter in an effort to provide a smoothed solution matrix for both temperature and atmospheric water content. This filtering process is based upon the knowledge that, in general, for large-scale footprints, both atmospheric water content and temperature are continuous functions and that they should be represented as such in the algorithm.

The convergence requirements are quite simple. After each iteration the values of f_i ($i = 1, 2, 3$) are compared with the previous iterations. When 99% of the points are stable to within some stability parameter ± 0.01, for all three f_i, then the algorithm stops and all parameter values are printed. This provides execution times of the order of 5 min for 25 iterations

on a VAX 11/750 computer. If the convergence requirements are changed, the algorithm could execute faster to provide a trade-off between execution time and uncertainties in the retrieved parameters.

In an effort to always find the least constrained physically realizable solution the algorithm progresses through four different levels of constraint. This solution tree is graphically shown in Figure 2. At the first level only λ_0 is applied, constraining the sum of f_i to be 1, while each of the other two Lagrange multipliers is forced to zero. If this level produces a solution within the valid retrieval triangle, and the composite wind value is positive, then these values will be assigned as the solution vector at this pixel for this iteration. Otherwise, if the solution is not within the valid retrieval triangle, the algorithm proceeds to level three where constraint λ_i is added to the solution while λ_1 is forced to zero. This constraint forces the surface vector (f_1, f_2, f_3) to lie on one of the edges of the triangle. If the composite wind value is negative at this level, then the fully constrained level four solution is attempted. This will force the solution to lie in the F space area, where it can be considered a physically meaningful solution. If at level one the only nonphysical output is the wind value, then the algorithm will apply the level two constraints λ_0 and λ_1. This will force the wind vector to zero but will still allow the surface vector to lie anywhere within the triangle. If a level two solution cannot be found, then the algorithm proceeds to level three as previously described.

The solution of the temperature vector starts at the solution of (4) in terms of T_s and $\langle T \rangle$ as follows:

$$T_b - T_c r e^{-2\tau_\infty} = (1 - e^{-\tau_\infty} + r(e^{-\tau_\infty} - e^{-2\tau_\infty}))\langle T \rangle + (1 - r)e^{-\tau_\infty} T_s \qquad (19)$$

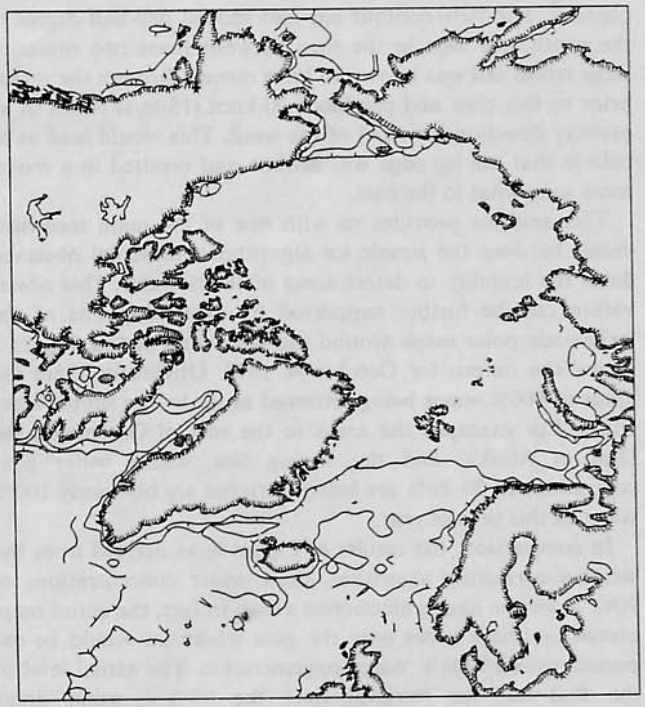

Fig. 5. Water contours as derived form the UMass-AES algorithm over the Arctic for October 4, 1978. The contours represent 90%, 80%, and 70% (hashed lines) water.

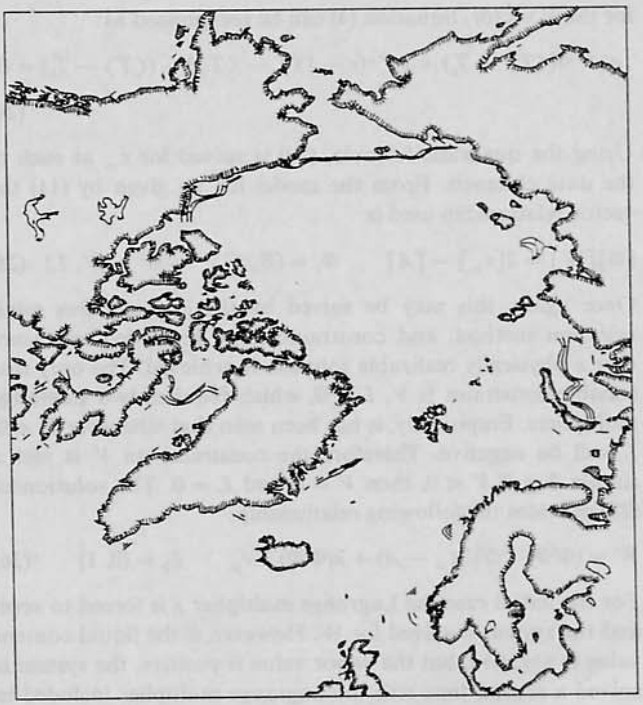

Fig. 6. Water contours as derived from the weather-correcting algorithm over the Arctic for October 4, 1978. The contours represent 90%, 80%, and 70% (hashed lines) water. The discontinuity in the ice edge northeast of Greenland in the Barents Sea represents missing data due to the inclination of the orbit.

Solving this for the multichannel case in a vector context we can represent

$$[T] = (T_s, \langle T \rangle)$$

$$[\beta]_i = (T_b - T_c r e^{-2\tau_\infty})_i$$

$$[\Psi]_i = (((1 - r)e^{-\tau_\infty}) \quad (1 - e^{-\tau_\infty} + r(e^{-\tau_\infty} - e^{-2\tau_\infty})))_i \qquad (20)$$

for data channel i. These vectors are related by the following expression:

$$[\beta] = [\psi] \cdot [T] \qquad (21)$$

Following the previous solution method, we arrive at the final equation for the solution of the temperature vector as

$$T = (\Psi^t \Psi)^{-1} \Psi^t \beta + \lambda (\Psi^t \Psi)^{-1} E \qquad (22)$$

where $E = (-a, 1)$. The Lagrange multiplier λ is used to constrain $\langle T \rangle$ to be a linear function of T_s of the form $\langle T \rangle = aT_s - b$. This is a particularly forgiving assumption because it has been shown [*Swift*, 1984] that a ± 50 K error in the estimate of atmospheric temperature is required to give a $\pm 5\%$ error in the retrieval of sea ice concentration. This constraint can be represented in vector form as follows:

$$[T] \cdot [E] = -b \qquad (23)$$

The algorithm as presented used values of $a = 1.08$ and $b = 37$, which are reasonable values for polar regions, where the atmospheric lapse rate generally is small.

Simultaneous with the solution of the temperature vector the attenuation due to atmospheric water vapor and liquid is evaluated. This system is also solved analagous to the solution

for the F vector. Equation (4) can be reexpressed as:

$$e^{-2\tau_\infty} r(\langle T\rangle - T_c) + e^{-\tau_\infty}(r-1)(T_s - \langle T\rangle) - (\langle T\rangle - T_b) = 0 \tag{24}$$

Using the quadratic formula, (24) is solved for τ_∞ at each of the data channels. From the model for τ_∞ given by (11) the vector relationship used is

$$[\Phi][W] = 2[\tau_\infty] - [A] \qquad \Phi_i = (B_i, C_i) \qquad W = (V, L) \tag{25}$$

Once again, this may be solved by the least squares minimization method, and constraints may be added to ensure that a physically realizable solution is achieved. The only reasonable constraint is V, $L \geq 0$, which requires two Lagrange multipliers. Empirically, it has been seen that whenever $V < 0$, L will be negative. Therefore the constraint on V is just a simple flag if $V < 0$, then $V = 0$ and $L = 0$. The solution of (25) provides the following relationship:

$$W = (\Phi^t\Phi)^{-1}\Phi^t(2\tau_\infty - A) + \lambda(\Phi^t\Phi)^{-1}\hat{e}_2 \qquad \hat{e}_2 = (0, 1) \tag{26}$$

For the initial case the Lagrange multiplier λ is forced to zero, and the system is solved for W. However, if the liquid content value is negative, but the vapor value is positive, the system is solved a second time wth the Lagrange multiplier included in the solution. This ensures a physically realizable value for the atmospheric water content.

Results From the Algorithm

For analysis of the algorithm, two different sets of Seasat SMMR data were processed. To verify the ability of the algorithm to provide data over large areas, a polar grid covering the northern hemisphere from latitude 45° north was used. This 76 × 52 grid provided 100-km² pixels of SMMR data averaged into 24-hour frames. For more detailed analysis of the actual performance of the algorithm, five single-orbit swaths over the Beaufort Sea were used. These data cover the period October 2–8, 1979, and consist of orbits 1395, 1409, 1438, 1452, and 1481. The single-swath data were gridded into 50-km² pixels. Total retrieval time for each channel is of the order of 5 min. For both sets of data the input channels used were 18-, 21-, and 37-GHz horizontal and vertical polarizations. All processed data for these orbits are published in an M.S. thesis [*Walters*, 1986].

Fig. 7. Atmospheric water vapor contours as derived from the weather-correcting algorithm over the Arctic for October 4, 1978. The contours represent 1, 2, 3 (hatched lines) and 4 g/cm² of integrated water vapor. The high concentration of water vapor in the North Atlantic Ocean and the Gulf of Alaska correlate with the false retrievals of sea ice shown in Figure 5. The false retrievals in the Bering Sea are a result of high winds in the area.

Many of the problems associated with the simple ice algorithms can be seen by the comparing of surface contour maps of their output. For example, Figure 3 shows the contours of open water concentration for orbit 1395 (October 2, 1978) as derived from the UMass-AES algorithm. We choose to plot water fraction because of the way our algorithm is structured; however, ice concentration is derived simply by subtracting the values shown from 100%. These contours start at 10% and continue up through 80%, leading us to believe that there are no areas with less than 10% ice on the surface. From the ice charts shown by *Swift et al.* [1985], aircraft observers have recorded no traces of ice in the western region, certainly far less than the 10% + recorded by the algorithm. This spurious ice is attributed to localized weather conditions, where the effects of both wind and atmospheric water vapor is to lower the apparent reflectivity of the surface. The simple algorithm will therefore tend to indicate more ice than is actually there. If we next consider the water contours for orbit 1481 (October 8, 1978), as shown in Figure 4, we can see interesting changes in the UMass-AES algorithm output. An important change is that the water contour with the greatest value is the 70% contour. The 70% contour has also moved one-half degree to the south and west in the time between these two orbits. A large storm cell was known to have moved through the region prior to this time and produced 30-knot (15-m/s) winds in an easterly direction for most of the week. This would lead us to believe that the ice edge was broken and resulted in a movement somewhat to the east.

This analysis provides us with one of the main inconsistencies between the simple ice algorithm and actual observed data: the inability to detect areas of 100% water. This observation can be further supported by examining one of the large-scale polar maps around the same time period. Figure 5 shows the output for October 4, 1978. Obviously, there are areas of 100% water being retrieved as ice by the simple algorithm. For example, the areas to the east of Greenland, the Gulf of Alaska, and the Bering Sea, where water concentrations of 70–80% are being retrieved are obviously 100% water at this time of year.

In comparison, the results of Figure 6, as derived from the weather-correcting algorithm, show water concentrations of 90% + for the above mentioned areas. In fact, the entire map, except for those areas near the pole where ice would be expected, shows 90% + water concentration. The actual level of the first-year ice retrieval over the 90% + water areas averages 3%. Thus the weather-correcting algorithm has reduced the ice concentration from 20 to 3% over largely open water areas. It is also of interest to note that the ice edge in the Kara Sea has been greatly enhanced by the algorithm and

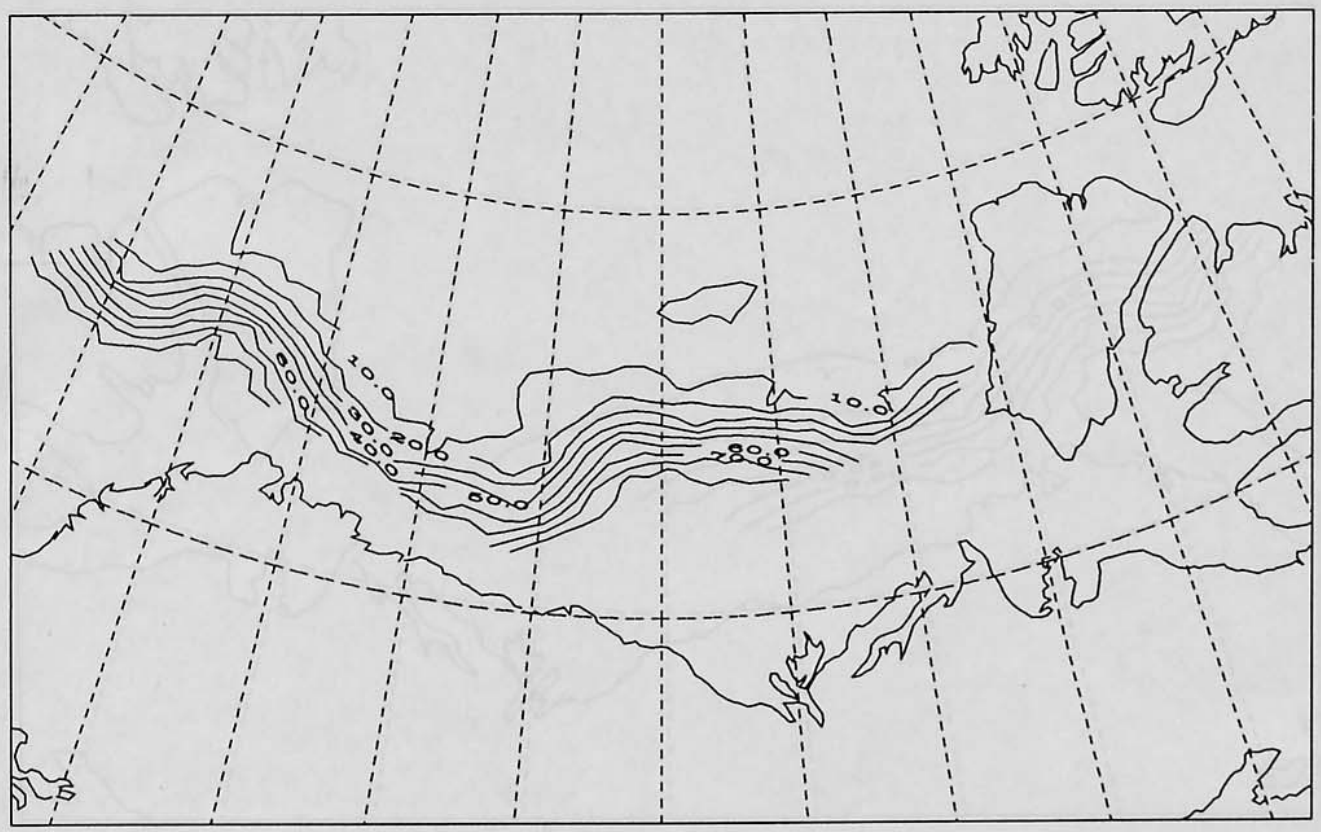

Fig. 8. Contours of surface water concentration as derived from the weather-correcting algorithm for Seasat orbit 1395 (October 2, 1978). The maximum concentration shown in the figure is 90% water. By comparing with the UMass-AES results given in Figure 3, the weather-correcting algorithm derives the 90% water contour and stretches the 10% water contour. Also shown is a 10% contour in the pack ice, a vestige of which appears in orbit 1409.

that the ice edge of the Barents Sea has disappeared into the polar region not observed by the Seasat SMMR.

Continuing the examination of the polar type output, Figure 7 shows the derived atmospheric water vapor levels for October 4. These retrievals range from near 0 g/cm^2 over the ice pack in the Beaufort Sea to 5 g/cm^2 over some areas of the open ocean. The large values of the relative atmospheric water vapor most likely correspond to stormy regions, as derived wind values for these areas are also relatively high.

For the single-orbit water contour maps shown in Figures 8 and 9 (orbits 1395 and 1481) the ability of the weather-correcting algorithm to resolve surface water, or total ice concentration, can be seen. Most of the features of these maps are similar to those seen in Figures 3 and 4 as derived from the simple UMass-AES algorithm, except for a few important differences. The greatest value of the contour line for both orbits is the 90% + line, and the entire range of contour lines from 50 to 90% covers a linear range of only one half degree. For orbit 1481 the lines are slightly farther apart than for 1395, but this would be expected if the passage of the storm broke up the ice edge. Once again, where the simple UMass-AES algorithm is retrieving 20% + first-year ice in an expected 90% + water region, the weather-correcting algorithm retrieves the expected 90% + water value. This contrast can be noted in Figure 10, which shows the fraction water plotted as a function of distance along pixel 7 in the SMMR track for repeat orbits 1395, 1438, and 1481, which crossed over multiyear ice near Banks Island, then over a region of high first-year ice concentration and finally, over the ice edge continuing to open water near Point Barrow. Results from both the simple UMass-AES algorithm and the weather-correcting algorithm are shown. Figures 10*a* and 10*b* again illustrate the property of the weather-correcting algorithm to identify areas that are void of sea ice. At first glance, this property may appear to be entirely forced by the Lagrange multipliers used to constrain the problem. However, the results of Figure 10*c* (orbit 1481) indicate that this may be true only for ice concentrations well below the 10% level. Recall that a storm passed over the area which probably caused significant redistribution of the sea ice cover prior to orbit 1481. Figure 10*c* indicates that this storm created a relatively diffuse ice edge with a sea ice concentration of 10% extending several footprints away from the pack.

Finally, we note that the weather-correcting algorithm predicts a 5% level of water fraction within the ice pack for orbit 1395. At the present it is not clear whether this is real or an artifact associated with potential errors in selecting the algorithm calibration points.

DISCUSSION

The weather-correcting sea ice algorithm is tailored to accept six SMMR channels (18H, 18V, 21H, 21V, 37H, and 37V) to produce six environmental parameters, namely, total ice concentration, multiyear ice fraction, surface temperature, ocean surface wind speed, integrated atmospheric water vapor, and cloud liquid water content. The absolute accuracy with

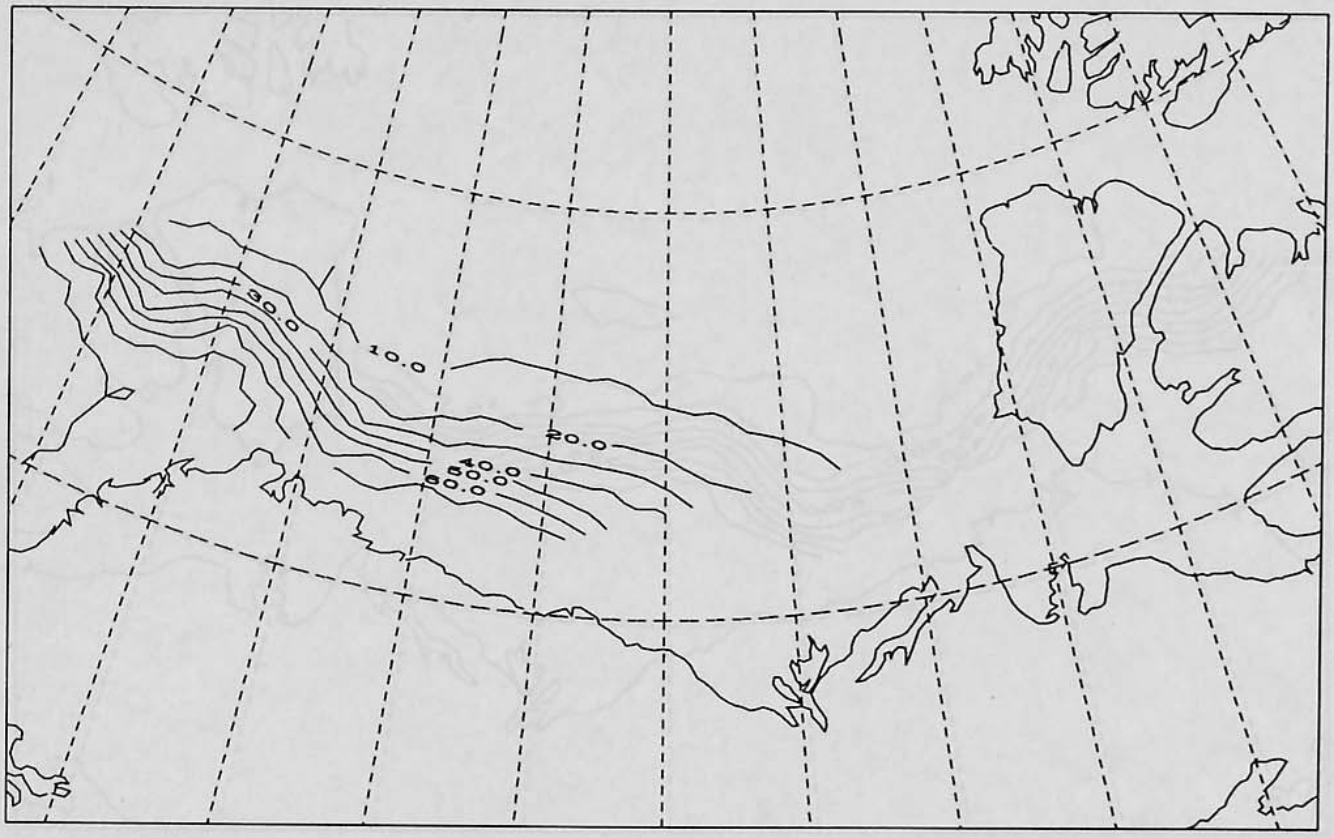

Fig. 9. Contours of surface water concentration as derived from the weather-correcting algorithm for Seasat orbit 1481 (October 8, 1978). The maximum concentration shown in the figure is 90% water.

which these parameters can be derived is associated with two factors. The first factor is the relationship between brightness temperature and a particular environmental parameter. Of the six parameters considered the atmospheric contributions are most accurately known as a result of exhaustive non-site-specific experimentation. Although the effects of changes in surface temperature are well known, a microwave radiometer measures the product of the surface temperature and the surface emissivity. We judge that the absolute accuracy of the emissive properties of sea ice and the wind-driven ocean surface are not sufficiently well bounded at this time. Such data is not only expensive to gather, but absolute results seem to vary from one investigator to another either because of natural variability, imperfect instrument calibration, or both. The uncertainties in instrument calibration is the other principal factor that imposes restrictions on the absolute accuracy of the retrievals. In the case of the Seasat SMMR, calibration errors were well recognized but never well defined. Furthermore, one of the channels was known to have experienced a change of 6 K in less than 24 hours.

In view of these two inherent problems, virtually all investigators, including ourselves, have attempted to correct for these systematic biases by establishing algorithm calibration points. Figure 1 illustrated this procedure as applied to the retrieval of sea ice parameters. The problem with this process is that the algorithm is tuned to retrieve sea ice parameters while accepting errors in all others that have not been subjected to such a tuning process. The effects of such errors were immediately evident to us in the retrieval of surface temperature. The surface temperatures produced over the Beaufort Sea ranged from 270 K over the ice pack to near 300 K over areas of open water. These higher values for ocean temperature are not physically realizable in the Arctic; however, they did correspond to an expected trend of lower temperatures over sea ice at northern latitudes and higher temperatures over open water to the south. As another example of retrieving reasonable relative values, the atmospheric water vapor contours shown in Figure 7 correlate with low-pressure cells identified on weather maps.

To compound these problems, it was discovered late in the review process of this paper that the $\sec\theta$ factor associated with the SMMR pointing angle was not included in the formula for increased atmospheric opacity ($\tau_\infty = \tau_\infty{}^0 \sec\theta$). This omission propagates a near factor of 2 error in an exponential. After discovery of the error the proper correction was added to the computer software, and the results were regenerated. The resultant changes in the sea ice retrievals were small, about 1%, which was not unexpected simply because the algorithm is tuned to retrieve sea ice. The major differences occurred in the absolute values retrieved for ocean surface wind speed, water vapor, and cloud liquid water content. As an indication of how the retrieved environmental parameters changed with the proper addition of the $\sec\theta$ factor, Table 4 gives the appropriate statistical parameters comparing values retrieved with and without the $\sec\theta$ factor. The y axis defines retrievals that include the $\sec\theta$ factor.

Comparisons with aircraft or ground-based surface observations are always desirable as a means to establish confidence in results obtained from satellite data. Although major field experiments were planned for Seasat, these programs never materialized because of the short lifetime of the satellite. In addition, the area over the Beaufort Sea had persistent cloud

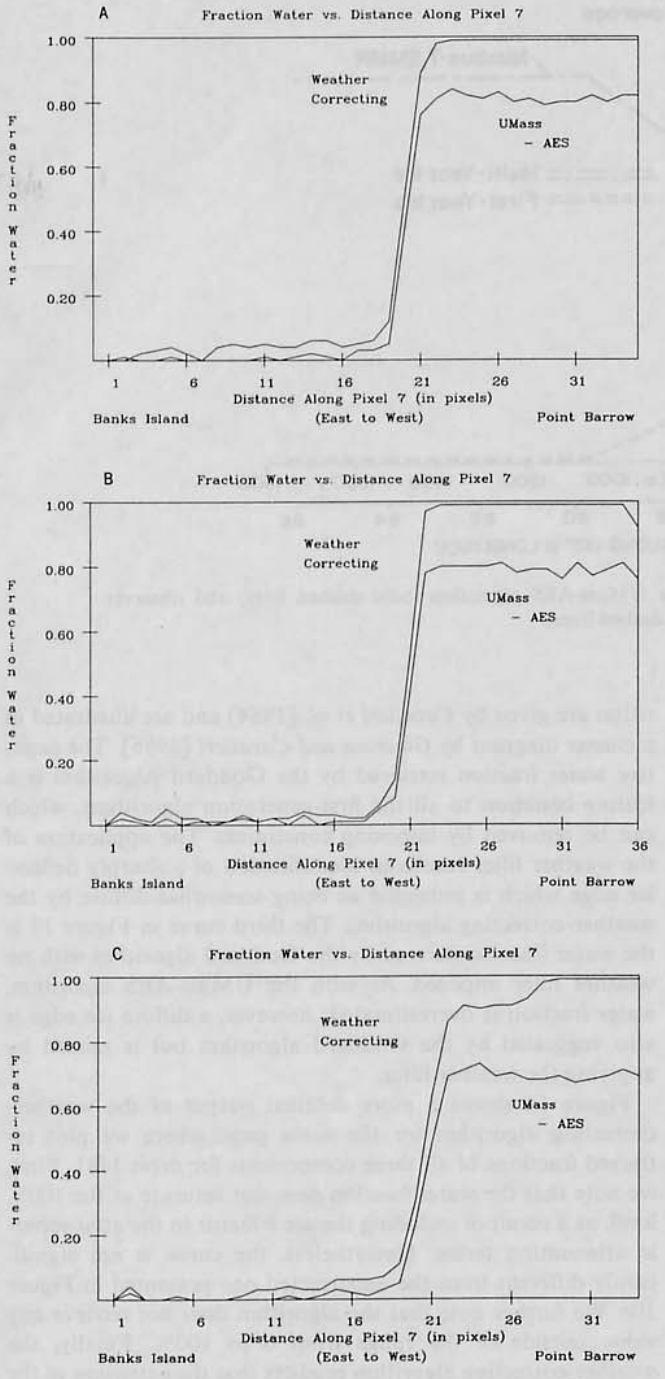

Fig. 10. Fraction of water as derived from the two algorithms versus distance along pixel 7 of the SMMR swath from Banks Island to Point Barrow (*a*) orbit 1395, (*b*) orbit 1438, (*c*) orbit 1481. These graphs further illustrate that the first-generation algorithms can underestimate water fraction by 20%. The weather-correcting algorithm also indicates the existence of a diffuse ice edge for Seasat orbit 1481.

cover after September 2, 1978, so that no usable satellite images were available. As a result, the prime comparative sets for analysis of the Seasat data were ice charts that are routinely issued by the Canadian Atmospheric Environment Service. The reader is referred to *Swift et al.* [1985] for a detailed discussion of the comparison. However, the principal conclusions drawn were that areas of predominately first-year sea ice were detected by the algorithm and that the 40% contour

TABLE 4. Statistical Comparisons of Retrievals Using Secθ Opacity Weighting (Y Axis) Versus Those Without Secθ (X Axis)

Environmental Parameter	Slope	Y Intercept	Correlation Coefficient
Multiyear ice, %	1.04	0.766	1.00
First-year ice, %	0.95	−0.596	1.00
Water, %	1.00	−0.692	1.00
Surface temperature, K	1.04	−10.47	0.99
Ocean surface wind speed, m/s	0.85	−0.50	0.85
Atmospheric water vapor, g/cm^2	0.65	0.00	0.99
Cloud liquid water, g/cm^2	0.98	0.00	0.98

of derived multiyear fraction generally follows the old ice contour of the ice chart. The major disagreement between the ice chart and the product derived by the UMass-AES algorithm was the resultant distribution of multiyear ice as derived from the algorithm. The AES ice chart shows an abrupt change in multiyear fraction from 0 to 100%, whereas all the first-generation algorithms indicate a much more gradual change within the pack that observers define simply as mostly old ice. Since all the algorithms give similar results, we conclude that the observed gradient is associated with the radiometry properties of sea ice.

The Nimbus 7 satellite was launched shortly after the failure of Seasat with an identical SMMR. This sensor, which is still functioning, provided another opportunity to evaluate the quality of sea ice algorithms. After modifying the equivalent reflectivities to adjust for different instrumental biases a field program was undertaken by the AES group to further validate the UMass-AES algorithm. As part of this field program, observers were requested to assign a better tolerance to their estimates than the 20% quantization levels that are normally used in developing the operational product. The results of the intercomparison between the observed and Nimbus-derived multiyear ice fractions are given by *Swift et al.* [1985] and are reproduced as Figure 11 in this paper. This figure shows results of an AES aircraft underflight of Nimbus 7 on February 12, 1979. Results derived from ice observers and the Nimbus 7 SMMR are compared as a function of distance along 135°W longitude in the Beaufort Sea. Both of the derived products follow a similar trend. The aircraft data indicate a much more abrupt change in the distribution of ice types, whereas the algorithm results in a smoother distribution. As pointed out by *Swift et al.* [1985], some of this smoothing may be associated with spatial averaging by the SMMR footprint; however, the UMass-AES algorithm now appears to underestimate multiyear ice concentration.

In order to compare the UMass-AES results of Figure 11 with results obtained from the weather-correcting algorithm, multiyear ice fraction for Seasat orbit 1481 was retrieved using both algorithms. The results are cross plotted in Figure 12. The limitation of the first-generation algorithm to provide accurate values of low ice concentration is clearly evident. When the weather correcting algorithm indicates no ice, the UMass-AES algorithm produces a residual concentration of almost 20%. The other major difference is that for multiyear ice concentrations exceeding 20% the weather-correcting algorithm produces a higher estimate. This higher estimate is in better agreement with the observer-derived multiyear ice fraction

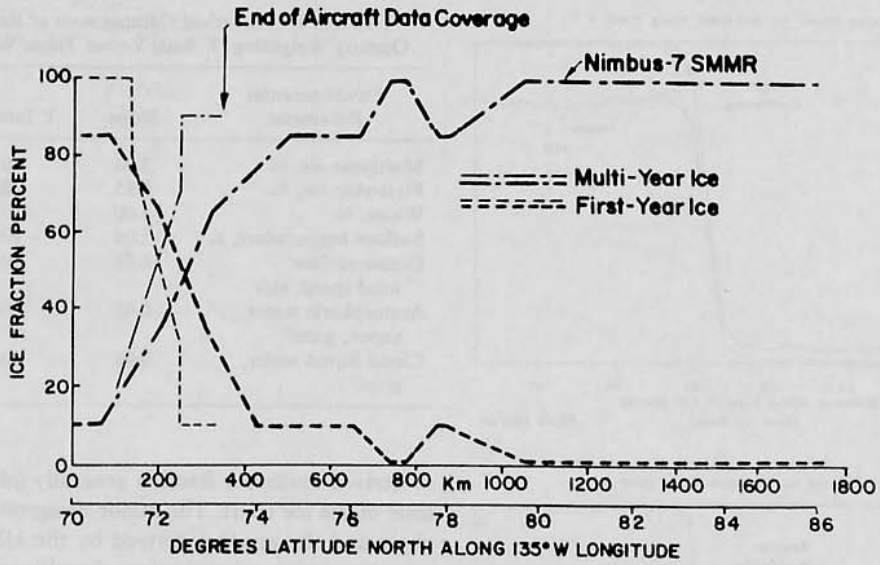

Fig. 11. Ice fractions along longitude 135°W, based on the UMass-AES algorithm (bold dashed lines) and observer estimates (light dashed lines).

shown in Figure 11. It therefore appears that the weather-correcting algorithm may yield a better data product. It is of interest to note that Figure 12 is not a linear relationship, which may suggest the influence of ice temperature in the weather-correcting algorithm.

Up to this point the weather-correcting algorithm has been compared with the UMass-AES algorithm, primarily because of the authors' involvement in verifying the quality of that particular first-generation algorithm. It is, however, appropriate to present at least one comparison with results obtained with the Goddard algorithm. Such a comparison is presented in Figure 13 for Seasat orbit 1481, where we show water fraction derived from the weather-correcting algorithm (including the sec θ term) and the Goddard algorithm with and without the weather filter. Calibration points for the Goddard algorithm are given by *Cavalieri et al.* [1984] and are illustrated in a cluster diagram by *Gloersen and Cavalieri* [1986]. The negative water fraction retrieved by the Goddard Algorithm is a feature common to all the first-generation algorithms, which can be removed by imposing constraints. The application of the weather filter results in identification of a sharply defined ice edge which is indicated as being somewhat diffuse by the weather-correcting algorithm. The third curve in Figure 13 is the water fraction derived by the Goddard algorithm with no weather filter imposed. As with the UMass-AES algorithm, water fraction is overestimated; however, a diffuse ice edge is also suggested by the Goddard algorithm but is missed by applying the weather filter.

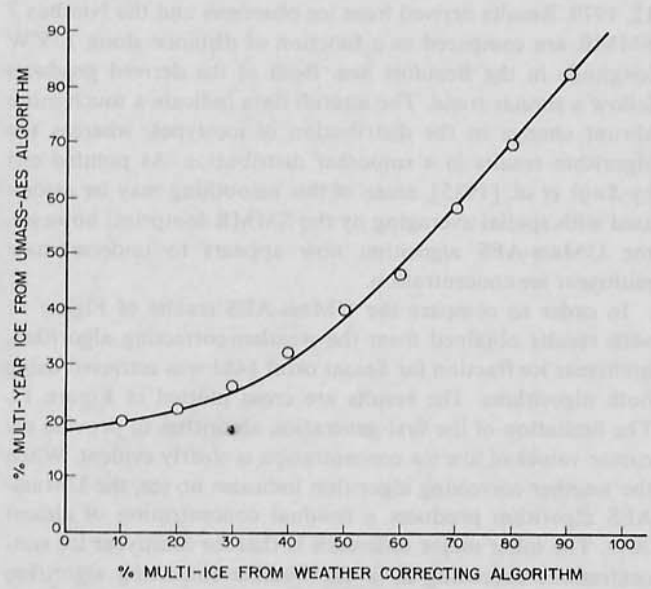

Fig. 12. Cross plot of multiyear sea ice derived from the UMass-AES and weather-correcting algorithms for Seasat orbit 1481.

Figure 14 shows a more detailed output of the weather-correcting algorithm for the same pass, where we plot retrieved fractions of all three components for orbit 1481. First, we note that the water fraction does not saturate at the 100% level, as a result of including the sec θ factor in the atmospheric attenuation terms. Nevertheless, the curve is not significantly different from the uncorrected one presented in Figure 10*c*. We further note that the algorithm does not retrieve any value outside of the range from 0 to 100%. Finally, the weather-correcting algorithm predicts that the extension of the ice edge is associated with multiyear floes that could have been released from the pack as a result of the storm. Such details are certainly masked by imposing a weather filter and would likely be dismissed using any of the first-generation algorithms because of the 80% + fractions of water derived over areas known to be open water.

Concluding Remarks

A weather-correcting sea ice algorithm has been developed which performs at least as well, if not better than, the first-generation UMass-AES algorithm, which was tested against field observations. Although first-generation algorithms, the Goddard one in particular, will satisfy the majority of the needs described by *Swift and Cavalieri* [1985], the weather-correcting algorithm has certain features which will be explored in connection with future satellite programs. First of

all, a natural method was developed to correct for weather and perhaps can be used to provide more additional environmental parameters. It also appears that some features are lost by application of the simple algorithms. For example, the simple UMass-AES algorithm did not detect the ice edge in the Kara Sea in the polar grid display for October 4, 1978. The new algorithm may also find use in studies of the marginal ice zone, where retrievals of low ice concentration are required. Future work will focus on gathering additional in situ data to better establish retrieval accuracies and means to better address the effects of instrument biases.

In the future, newer, more precise radiometers will be used, and the performance of the algorithm should be improved. Simultaneous advances in the computer field and rewriting of the software should make the cost of the data analysis much lower than the present. In this light, some possible future advances in the foregoing research will be mentioned.

One of the major problems with the data used for this research is the instrument biases in the SMMR. Several different approaches to correcting these have been used; however, there is no way to verify independently that any of these methods actually work. In general, these approaches have been verified by generating the expected output. In this way, some instrument biases have been corrected, but there are no guarantees that all biases have been eliminated. These biases have caused errors in the retrieval of the secondary environmental parameters but have proven to be forgiving, as evidenced by the small errors in retrieving sea ice fractions.

Use of the upcoming Special Sensor Microwave/Imager (SSM/I) for data acquisition should provide a much more sound body of data for input to the algorithm. Surface truth measurements should be available, as well as improved calibration techniques and improvements in the actual instruments themselves. The SSM/I is missing the 21-GHz horizontal channel; however, it does have two channels at 85 GHz available. On the basis of the loss of one of the channels used in the weather-correcting algorithm, one of the degrees of freedom of the solution will have to be removed until confidence in the use of the 85-GHz channels is achieved. On the basis of the low values of liquid water retrieval in the Arctic it would seem that the atmospheric liquid could be set to zero. Such a change would make the algorithm applicable to the SSM/I program without the 85-GHz channels until confidence is developed to use these channels.

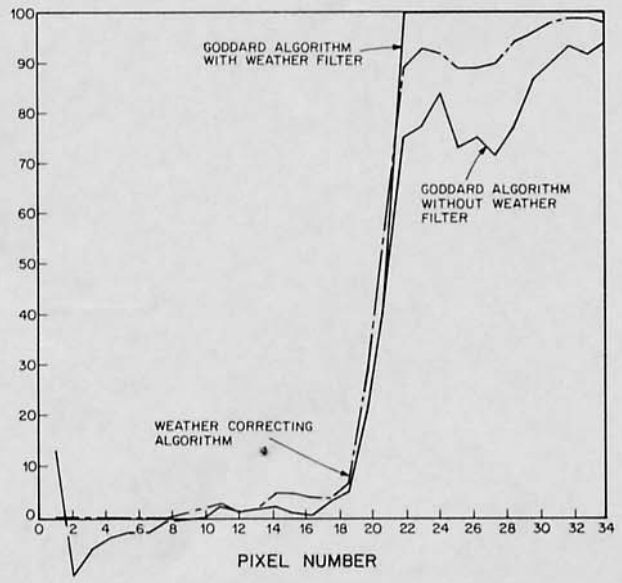

Fig. 13. Water fraction derived for the weather-correcting algorithm and the Goddard algorithm with and without the weather filter. The data are plotted along pixel 7 of the SMMR swath for Seasat orbit 1481.

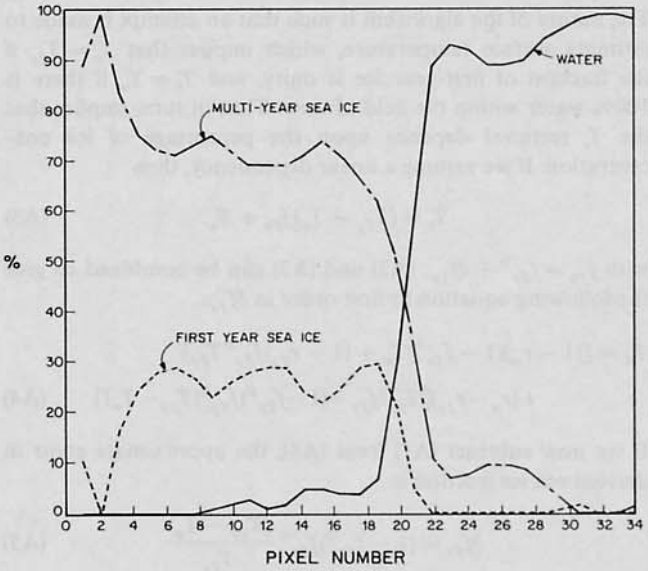

Fig. 14. Water, multiyear ice, and first-year ice fraction as derived from the weather-correcting algorithm. The data are plotted along pixel 7 of the SMMR swath for Seasat orbit 1481.

One aspect of some of the ice algorithms not addressed so far is the use of a high-resolution mode based on the two highest-frequency channels for more accurate resolution of the ice edge. This type of mode could be woven into the weather-correcting sea ice algorithm as an added feature. These channels could be used to create an ice edge detection mode with an even higher resolution than the previously used 37-GHz channels.

Graphs for all retrievals for Seasat orbits, 1395, 1409, 1438, 1452, and 1481, scatter plots, and a listing of the computer program, complete with flow charts, are given by *Walters* [1986].

APPENDIX

In this section we estimate the error in derived sea ice fractions resulting from the assumption that ice and water assume the same temperature within the field of view of the radiometer. To simplify the analysis, we will assume that there is no multiyear ice, so that the composite surface brightness temperature is given by:

$$T_B = (1 - r_w) f_w{}^0 T_w + (1 - r_{fy}) f_{fy}{}^0 T_{fy}$$
$$= (1 - r_w)(1 - f_{fy}{}^0) T_w + (1 - r_{fy}) f_{fy}{}^0 T_{fy} \qquad \text{(A1)}$$

where T_w and T_{fy} are the true surface temperatures of water and ice, respectively. The superscripts on the fractions indicate true fractions. The development of (7) assumes that $T_w = T_{fy} = T_s$, where T_s is an assumed isotropic surface temperature, such that

$$T_B = [(1 - r_w)(1 - f_{fy}) + (1 - r_{fy}) f_{fy}] T_s \qquad \text{(A2)}$$

The nature of the algorithm is such that an attempt is made to estimate surface temperature, which implies that $T_s = T_{fy}$ if the fraction of first-year ice is unity, and $T_s = T_w$ if there is 100% water within the field of view. This, in turn, implies that the T_s retrieval depends upon the percentage of ice concentration. If we assume a linear dependency, then

$$T_s = (T_{fy} - T_w)f_{fy} + T_w \tag{A3}$$

with $f_{fy} = f_{fy}{}^0 + \delta f_{fy}$; (A2) and (A3) can be combined to give the following equation to first order in δf_{fy}:

$$T_B = [(1 - r_w)(1 - f_{fy}{}^0)T_w + (1 - r_{fy})f_{fy}{}^0 T_{fy}] + (r_w - r_{fy})[T_{fy}\delta f_{fy} - (1 - f_{fy}{}^0)f_{fy}{}^0(T_{fy} - T_w)] \tag{A4}$$

If we now subtract (A1) from (A4), the approximate error in derived sea ice fraction is

$$\delta f_{fy} = (1 - f_{fy}{}^0)f_{fy}{}^0 \frac{(T_{fy} - T_w)}{T_{fy}} \tag{A5}$$

There is no error when $f_{fy}{}^0$ is either zero or one, and the maximum error occurs when $f_{fy}{}^0 = 1/2$. For $T_{fy} = 270$ K,

$$\delta f_{fy} = 0.0009(T_{fy} - T_w) \tag{A6}$$

Therefore a 5% error in derived concentration occurs when there is a 50 K difference in the ice water temperature. We therefore conclude that our assumption contributes negligible retrieval error.

Acknowledgments. This research was supported by the National Aeronautics and Space Administration under grant NAGW-559. We are indebted to Frank Carsey and John Crawford of the Jet Propulsion Laboratory for supplying the polar-gridded Seasat SMMR data tapes and to Don Cavalieri for his thorough review of the paper. We also appreciate the efforts of David Choi of the University of Massachusetts for regenerating data after the error in atmospheric opacity was discovered.

REFERENCES

Cavalieri, D. J., P. Gloersen, and W. J. Campbell, Determination of sea ice parameters with the Nimbus 7 SMMR, *J. Geophys. Res., 89*, 5355–5369, 1984.

Comiso, J. C., Sea ice effective microwave emissivities from satellite passive microwave and infrared observations, *J. Geophys. Res., 88*, 7686–7704, 1983.

Gloersen, P., and F. T. Barath, A scanning multichannel microwave radiometer for NIMBUS-G and SEASAT-A, *IEEE J. Oceanic Eng., OE-2*, 172–178, 1977.

Gloersen, P., and D. J. Cavalieri, Reduction of weather effects in the calculation of sea ice concentration from microwave radiometers, *J. Geophys. Res., 91*, 3913–3919, 1986.

Klein, L. A., and C. T. Swift, An improved model for the dielectric constant of sea water at microwave frequencies, *IEEE J. Oceanic Eng., OE-2*, 104–111, 1977.

Svendsen, E., K. Kloster, B. Farrelly, O. M. Johannessen, J. A. Johannessen, W. J. Campbell, P. Gloersen, D. Cavalieri, and C. Matzler, Norwegian Remote Sensing Experiment: Evaluation of the Nimbus 7 Scanning Multichannel Microwave Radiometer for sea ice research, *J. Geophys. Res., 88*, 2781–2791, 1983.

Swift, C. T., Sea ice algorithm error analysis, report, Dep. of Electr. and Comput. Eng., Univ. of Mass., Amherst, August 1984.

Swift, C. T., and D. J. Cavalieri, Passive microwave remote sensing for sea ice research, *Eos Trans. AGU, 66*, 1210–1212, 1985.

Swift, C. T., L. S. Fedor, and R. O. Ramseier, An algorithm to measure sea ice concentration with microwave radometers, *J. Geophys. Res., 90*, 1087–1099, 1985.

Walters, J. M., A weather correcting sea ice algorithm, M.S. thesis, Univ. of Mass., Amherst, 1986.

Wentz, F. J., A model function for ocean microwave brightness temperatures, *J. Geophys. Res., 88*, 1892–1908, 1983.

Wilheit, T. T., and A. T. C. Chang, An algorithm for retrieval of ocean surface and atmospheric parameters from observations of the Scanning Multichannel Microwave Radiometer, *Radio Sci., 15*, 525–544, 1980.

C. Ruf, C. T. Swift, and J. M. Walters, Department of Electrical and Computer Engineering, University of Massachusetts, Amherst, MA 01003.

(Received July 31, 1986;
accepted February 20, 1987.)